Ultrasonic tomographic imaging of temperature and flow fields in gases using air-coupled capacitance transducers

William M. D. Wright[a)]
Department of Engineering, University of Warwick, Coventry CV4 7AL, United Kingdom

David W. Schindel
Institute for Aerospace Research, NRC, Montreal Road, Ottawa, Ontario K1A 0R6, Canada

David A. Hutchins and Peter W. Carpenter
Department of Engineering, University of Warwick, Coventry CV4 7AL, United Kingdom

Dion P. Jansen
Ontario Hydro Technologies, Toronto, Ontario M8Z 5S4, Canada

(Received 25 July 1997; revised 5 August 1998; accepted 18 August 1998)

A pair of air-coupled ultrasonic capacitance transducers with polished metal backplates have been used to image temperature and flow fields in gases using ultrasonic tomography. Using a filtered back-projection algorithm and a difference technique, cross-sectional images of spatially variant changes in ultrasonic attenuation and slowness caused by the presence of temperature and flow fields were reconstructed. Temperature fields were produced in air by a commercial soldering iron, and the subsequent images of slowness variations used to reconstruct the air temperature at various heights above the iron. When compared to measurements made with a thermocouple, the tomographically reconstructed temperatures were found to be accurate to within 5%. The technique was also able to resolve multiple heat sources within the scan area. Attenuation and velocity images were likewise produced for flow fields created by an air-jet from a 1-mm-diam nozzle, at both 90 and 45 degrees to the scanning plane. The fact that temperature and flow fields can be measured in a gas without the need to insert any measuring devices into the image region is an advantage that may have many useful applications.
[S0001-4966(98)00412-3]

PACS numbers: 43.58.Dj, 43.35.Zc, 43.38.Bs, 43.60.Rw [SLE]

INTRODUCTION

Tomographic reconstruction[1] is a well-established imaging technique that allows spatial variations of a physical variable in a material to be determined using only measurements made at the periphery of the area of interest. This may be accomplished by propagating ultrasonic waves or x-rays through the material in many different directions in the imaging plane, and using information extracted from this data to reconstruct a cross-sectional image. In the case of ultrasonic tomography, measurements of wave amplitudes and propagation delays are usually used to produce cross-sectional images of ultrasonic attenuation and slowness. These acoustic properties are in turn related to other material properties of interest, such as temperature or flow velocity, as will be demonstrated in this work.

Ultrasonic tomographic imaging has already been widely investigated, especially for the inspection of solid materials such as silicon dioxide ingots,[2] wood,[3] and solid rocket propellants.[4] Techniques for speeding up the collection of data have also been studied, including automated data acquisition[5–7] and noncontact wave transduction.[8–11] One promising form of noncontact transduction is the air-coupled ultrasonic transducer,[12–14] in which ultrasonic energy is coupled to a material through an intervening air layer. Such transducers have been shown recently by the authors to be well suited for noncontact tomographic imaging of solids.[15]

Ultrasonic tomography has not yet been extended in any appreciable way to the characterization and imaging of gases themselves, which may be due in part to the lack of suitable gas-coupled transducers in the past. However, the air-coupled ultrasonic capacitance transducers used previously by the authors for noncontact tomographic inspection of solids[15] are ideally suited for developing tomographic imaging applications within gases themselves. As a direct result of their ability to generate and receive ultrasonic waves in gases over a large frequency bandwidth ($<$100 kHz to 2.25 MHz), these devices are ideal for accurate measurements of propagation delay and frequency content. It will be shown in the work to be described here that such broadband air-coupled transducers can now be used to image temperature and flow fields in gases using ultrasonic tomographic imaging.

I. THE TOMOGRAPHIC RECONSTRUCTION THEOREM

Of the two main types of algorithm used to reconstruct cross-sectional images from boundary data, iterative techniques or series expansion methods are the most popular.[16–19] The widespread use of these algorithms arises

[a)]Now at Department of Electrical Engineering and Microelectronics, University College Cork, College Road, Cork, Ireland.

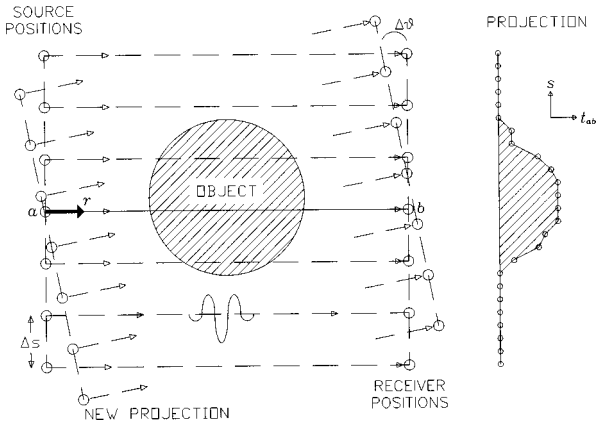

FIG. 1. The tomographic scanning geometry.

from their ability to correct for ray bending, anisotropy, and irregular sampling geometries, although such methods are computationally intensive. Transform methods[20–23] which use Fourier analysis are quicker and more efficient, but are not as versatile and require a precise sampling geometry. For this reason, Fourier transform methods have been less popular. In the work to be presented here, a filtered back-projection algorithm using Fourier transforms was used to reconstruct tomographic images. This method has been described in detail elsewhere,[23] but for completeness a brief outline of the technique will be given.

Consider the sampling geometry shown in Fig. 1, where an ultrasonic source and receiver with a fixed separation *ab* are scanned together in a linear path over the object to be imaged. At regular spatial intervals Δs, a waveform or ''ray'' is recorded by the receiver and the source–receiver propagation time-delay t_{ab} is extracted to form one point on a ''silhouette'' or projection at an angle θ through the center of the object (the projection in Fig. 1 plots the result for $\theta=0$). Assuming a linear ray path along *ab*, the propagation delay t_{ab} is given by

$$t_{ab}=\int_{r_a}^{r_b}\frac{dr}{c_r}, \tag{1}$$

where c_r is the sound speed at any distance r along *ab*. The integrand is more commonly known as the slowness. When a single projection has been completed, the transducer pair (or the object of interest) is then rotated through small angular increments $\Delta\theta$, and the scanning process repeated at each angle so that a series of projections is built up, each one passing through the center of the object like the spokes of a wheel. When a full 180 degrees has been scanned, the projections may then be reconstructed into a cross-sectional image of all the slowness variations anywhere within the scan area.

The projection theorem states that the one-dimensional Fourier transform of a projection passing through the object at an angle θ is equal to a section through the two-dimensional Fourier transform of the slowness function at the same angle. By substitution and manipulation, this reduces to a filtered back-projection which is a simple convolution of each projection with a kernel function in the Fourier domain. If data is then taken in specific geometries, the result of applying the filtered back-propagation algorithm is an image showing spatial variations in slowness. Although tomographic imaging has been described in terms of propagation delays and slowness function, other acoustic wave properties such as signal amplitude and frequency content can be used to reconstruct images of other useful functions such as attenuation, as will be demonstrated.

II. TOMOGRAPHIC IMAGING IN CASES

In the specific case of ultrasonic tomographic imaging of the properties of a gas, the ''object'' in Fig. 1 may consist of a region with either (a) an appreciable flow velocity, (b) a variation in the local sound speed (e.g., due to a change in temperature or pressure), or (c) a combination of both (a) and (b). To consider these effects, the effective sound speed c_e at any distance r along the line *ab* between the source and receiver may be given approximately by

$$c_e=c_r+\underline{\mathbf{v}}\cdot\hat{\mathbf{r}}, \tag{2}$$

where c_r is the local sound speed, $\underline{\mathbf{v}}$ is the local flow velocity of the gas (a vector quantity), and $\hat{\mathbf{r}}$ is a unit vector parallel with the ray path and pointing in the direction of integration. The dot-product in Eq. (2) ensures that the appropriate component of flow velocity will be added to, or subtracted from the local sound speed. Note that at high flow velocities, c_r will also vary with the gas flow speed, and so Eq. (2) is a linear approximation which is reasonably accurate provided that $|\underline{\mathbf{v}}|\leqslant 0.3c$.

With a substitution of Eq. (2), Eq. (1) thus becomes

$$t_{ab}=\int_{r_a}^{r_b}\frac{dr}{c_r+\underline{\mathbf{v}}\cdot\hat{\mathbf{r}}}, \tag{3}$$

which shows that the propagation delay t_{ab} will vary with spatial variations in both the local sound speed and gas flow velocity. Since the local sound speed c_r is known to vary with temperature according to

$$c_r=331.31\sqrt{\frac{T}{273.16}}, \tag{4}$$

where T is the air temperature in degrees Kelvin,[24] spatial variations in air temperature may also be extracted from the information contained in the measurements of propagation delay.

In most ultrasonic tomography experiments, absolute measurements of propagation delay or signal amplitude along known ray paths are usually required for the reconstruction of images. However, unknown delays and attenuation effects may be introduced by the pulser/receiver, while the exact propagation path between the source and receiver may be difficult to determine. In order to reduce the effect of such uncertainties, a form of difference tomography was employed in this work, in which the values obtained from each ray were normalized with respect to the first ray in each projection (taken in a region of ambient temperature and negligible flow velocity). In this way, a comparative image would be formed of only the *changes* in a physical variable induced by the presence of local sound speed variations or flow effects.

In the present application, comparative measurement can be included by rewriting Eq. (3) in the following form:

$$t_{ab}-t_{\mathrm{ref}}=\int_{r_a}^{r_b}\frac{dr}{c_{\mathrm{ref}}+\Delta c_r+(\underline{\mathbf{v}}_{\mathrm{ref}}+\Delta\underline{\mathbf{v}})\cdot\hat{\mathbf{r}}}-\int_{r_a}^{r_b}\frac{dr}{c_{\mathrm{ref}}+\underline{\mathbf{v}}_{\mathrm{ref}}\cdot\hat{\mathbf{r}}}, \tag{5}$$

where c_{ref} and $\underline{\mathbf{v}}_{\mathrm{ref}}$ are the values of c_r and $\underline{\mathbf{v}}$ corresponding to the first ray in each projection, and Δc_r and $\Delta\underline{\mathbf{v}}$ are the deviations from those values found at r along ab. Provided that $|\Delta c_r+\Delta\underline{\mathbf{v}}\cdot\hat{\mathbf{r}}|\ll|c_{\mathrm{ref}}+\underline{\mathbf{v}}_{\mathrm{ref}}\cdot\hat{\mathbf{r}}|$, then to a good approximation Eq. (5) further reduces to

$$t_{ab}-t_{\mathrm{ref}}\approx-\int_{r_a}^{r_b}\frac{\Delta c_r+\Delta\underline{\mathbf{v}}\cdot\hat{\mathbf{r}}}{(c_{\mathrm{ref}}+\underline{\mathbf{v}}_{\mathrm{ref}}\cdot\hat{\mathbf{r}})^2}dr, \tag{6}$$

which describes what will actually be recorded in the experiments to follow.

In many applications of practical interest, the flow effects can be considered negligible such that $|\underline{\mathbf{v}}_{\mathrm{ref}}|\ll c_{\mathrm{ref}}$ and $|\Delta\underline{\mathbf{v}}_r|\ll\Delta c_r$. In such cases, Eq. (6) may be simplified to

$$t_{ab}-t_{\mathrm{ref}}\approx-\frac{1}{c_{\mathrm{ref}}^2}\int_{r_a}^{r_b}\Delta c_r\,dr, \tag{7}$$

where it has been assumed that the reference ray is chosen well away from the region containing sound-speed variations. Equation (7) shows that a distribution in sound-speed variation can, in principle, be imaged by means of ultrasonic topography. One specific example in this case is the variation in sound speed due to the existence of a temperature field in air, where slowness variations may be converted to a reconstruction of the actual temperature field using Eqs. (7) and (4).

There are also many gas flows of practical interest where $|\Delta\underline{\mathbf{v}}_r|\gg|\Delta c_r|$, i.e., where the variations in local sound speed are negligible. In such cases, Eq. (6) reduces to

$$t_{ab}-t_{\mathrm{ref}}\approx-\int_{r_a}^{r_b}\frac{\Delta\underline{\mathbf{v}}\cdot\hat{\mathbf{r}}}{(c_{\mathrm{ref}}+\underline{\mathbf{v}}_{\mathrm{ref}}\cdot\hat{\mathbf{r}})^2}dr, \tag{8}$$

which shows how tomographic reconstruction of a flow field in a gas should also be feasible using only measurements made around the periphery of the flow. It is important to point out, however, that not all flow velocity fields can be uniquely reconstructed using equations such as Eq. (8).[25,26] The flow field must be ''divergenceless'' (which means that the flow-velocity field must satisfy $\nabla\cdot\underline{\mathbf{v}}=0$). Such a divergenceless flow field is ensured when the fluid is incompressible and has no sources or sinks of flow within the image plane. However, as air is a compressible fluid, not all flow velocity fields in air can be uniquely reconstructed using ultrasonic tomographic methods,[25] although reconstruction of other flow parameters such as vorticity is still possible.[26–28]

In the preceding equations, only the expected effects of temperature and flow on propagation delays have been considered, yet the amplitude of the ultrasonic waves will also be affected as they traverse the temperature- or flow-affected region. A sound wave traveling through a gas flow may be diverted from a direct path between the source and receiver by flow velocity components acting in directions perpendicular to the wave propagation. Similarly, temperature variations causing a local change in sound speed (and also gas density and specific acoustic impedance) will produce nonlinear ray paths and divert further sound energy away from the receiver. Rather than developing mathematical relationships for each amplitude effect, their effects will simply be discussed as they become apparent in the work to be described.

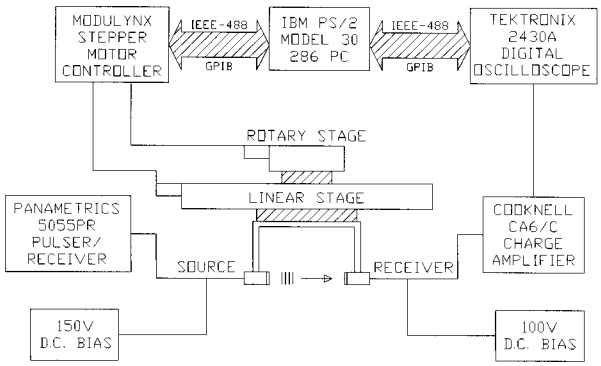

FIG. 2. Schematic diagram of the tomographic scanning equipment.

III. THE SCANNING SYSTEM

The experimental apparatus used for tomographic imaging in air is shown schematically in Fig. 2. Ultrasonic waves were both generated and detected in air using a pair of capacitance-type air-coupled transducers.[12] Each transducer consisted of a thin polymer film (2.5-μm-thick Mylar) which was placed upon a brass backplate whose surface had been polished to a roughness R_a of 0.02 μm. The upper surface of the Mylar film was metallized so that a capacitive structure was formed with the conducting backplate, to which a bias voltage was applied. In order to generate ultrasound in air, a transient voltage was superimposed upon the bias voltage, causing motion of the film via electrostatic forces; similarly, when acting as an ultrasonic receiver, an incident ultrasonic wave in air caused the film to move and vary the charge upon the backplate of the capacitive structure. Both the transmitting and receiving transducers had a 10-mm-diam aperture, which will have an effect on the spatial resolution of the reconstructed images, due to averaging of the signal across the transducer aperture in both the horizontal and vertical directions.

The air-coupled capacitive source was driven by a Panametrics 5055PR pulser/receiver, which delivered -250-V transients with a rise time of <10 ns. A dc bias voltage of 150 V was superimposed upon this transient voltage using a capacitive decoupling circuit. Received signals, resulting from charge variations at the air-coupled receiver, were detected using a Cooknell CA6/C charge amplifier. This charge amplifier had a sensitivity of 250 mV/pC, and applied its own well-regulated dc bias voltage of 100 V. The resulting output waveforms were captured on a Tektronix 2430A digital oscilloscope, and then transferred via an IEEE-488/GPIB

interface to an IBM PS/2 model 30 286 computer. This computer was also used to position the transducer pair using rotary and linear Daedal stages, which were driven by a Modulynx stepper-motor controller. The positioning system had an overall precision of ± 0.01 mm per 50 mm of travel. The distance between the source and receiver was fixed at 165 mm, whereas the height of the scanning plane could be manually altered. Unless stated otherwise, the dimensions of each scan were 100 mm in 2-mm steps and 180 degrees in steps of 3 degrees, giving 61 projections of 51 rays each.

IV. EXPERIMENTAL RESULTS AND DISCUSSION

A. Imaging temperature fields in air

In order to verify that the effects of temperature in a gaseous medium could be tomographically imaged (i.e., when $|\underline{\mathbf{v}}_{\mathrm{ref}}| \ll c_{\mathrm{ref}}$ and $|\Delta \underline{\mathbf{v}}_r| \ll |\Delta c_r|$), a temperature field was created in air above a 15-W miniature soldering iron, and the ultrasonic slowness field was imaged using tomographic reconstruction. The soldering iron, whose long axis had been clamped vertically in the center of the scan area, was insulated cylindrically using flexible glass-fiber high-temperature sleeving so that only the top 1-mm length of the 3.5-mm-diam tip was protruding. The soldering iron had a constant tip temperature of 340 °C.

Typical waveforms obtained in this arrangement are shown in Fig. 3(a), with the signal traveling through the heated column of air (dashed line) being lower in amplitude than the signal traveling through the surrounding ambient atmosphere (solid line). This reduction in amplitude of the ray passing through the heated air is attributed to a combination of refraction of the waves away from the receiver, and the mismatch in specific acoustic impedance between the heated air and the ambient atmosphere. From property tables[29] and Eq. (4), the specific acoustic impedance of air can be shown to change from 480 $\mathrm{kg \cdot m^{-2} \cdot s^{-1}}$ to 354 $\mathrm{kg \cdot m^{-2} \cdot s^{-1}}$ for a change in air temperature from 300 K to 400 K, respectively. This corresponds to a reflection coefficient at the interface between the heated and ambient regions of 0.5%. Diffraction of the waves will also have occurred as the diameter of the air column above the soldering iron (approximately 3.5 mm) was only five times the wavelength in air at the frequencies of interest (at 500 kHz, $\lambda = 0.7$ mm). Note that the heated wave also arrives sooner since the ultrasonic velocity is higher in the heated air as predicted by Eq. (4). The corresponding normalized frequency spectra obtained from these waveforms are shown in Fig. 3(b), where it can be seen that the frequency content of the heated wave has also reduced slightly. This was also attributed in part to refraction of the wave through the heated air which would cause the higher frequencies to arrive at an angle (i.e., incoherently) across the receiver aperture.

A full tomographic reconstruction of the soldering iron temperature field was also produced, using waveforms taken in a horizontal plane at a height of 10 mm above the vertical tip. The results may be seen in Fig. 4(a) for signal amplitude ($\mathrm{dB \cdot mm^{-1}}$) and Fig. 4(b) for slowness ($\mathrm{ns \cdot mm^{-1}}$). It is evident that the area immediately above the tip was most affected, as would be expected from a rising column of hot air.

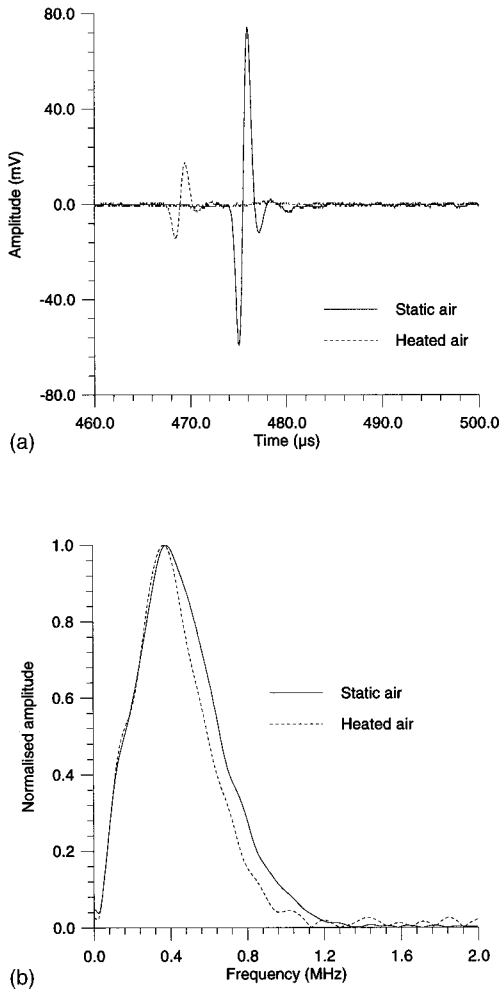

FIG. 3. (a) Typical waveforms through static air (solid line) and heated air (dashed line). (b) Normalized frequency spectra of waveforms shown in (a).

The fact that the amplitude image in Fig. 4(a) shows a larger affected area suggests that the ultrasonic amplitude is more susceptible to refraction and aperture effects than the propagation delays used to reconstruct the slowness image. The attenuation images thus complement the slowness images by indicating the presence of a temperature affected area which may not necessarily produce a measurable change in arrival time. Note that values of attenuation greater than zero are obtained in Fig. 4(a) due to noise both in the experimentally acquired acoustic data, and in the reconstruction algorithm. To minimize this effect, a Hamming window was used in conjunction with the kernel function in the filtered backprojection algorithm.

1. Effects of temperature-driven convective flow

It is important to point out that the soldering iron will produce a column of hot air that will be rising vertically due to convective (or buoyancy) forces.[30] This temperature-driven convective flow field may have an effect on the reconstructed tomographic images, an effect that is independent of the temperature effects already discussed. A simple theoretical calculation[30] was therefore used to predict the maximum vertical flow velocity due to natural convection for a cylindrical heat source of 3.5-mm diameter, with a con-

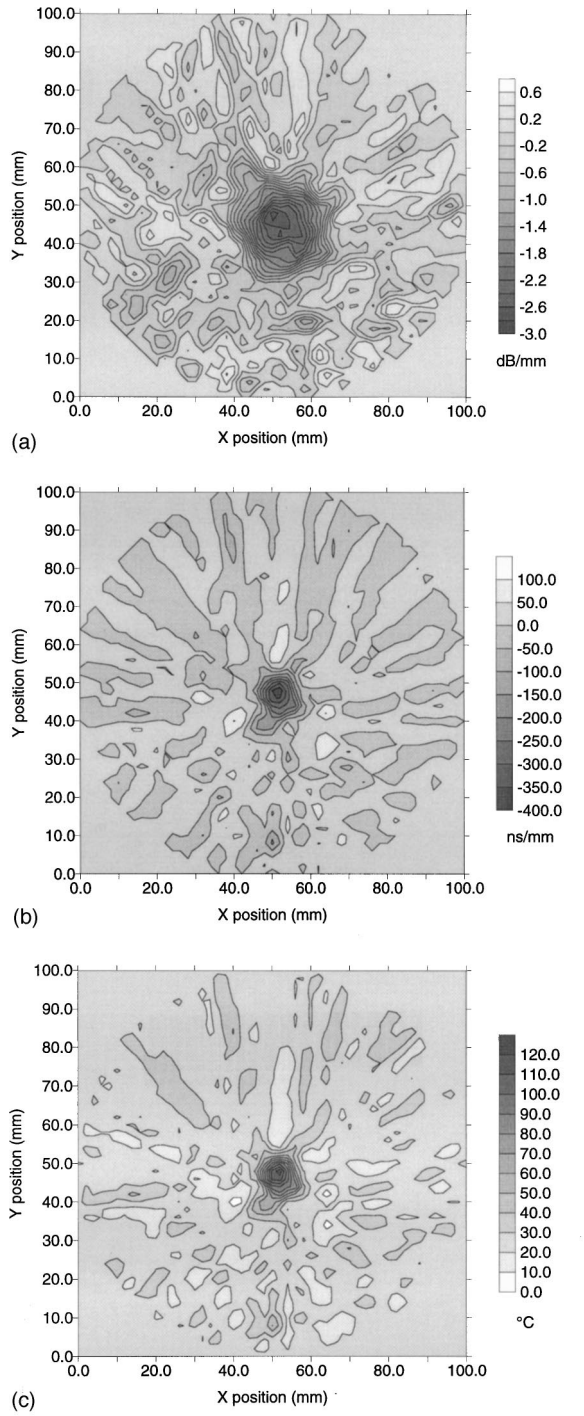

FIG. 4. (a) Attenuation image in $dB \cdot mm^{-1}$, (b) slowness image in $ns \cdot mm^{-1}$, and (c) temperature image in °C, taken 10 mm above a vertical 15-W soldering iron.

stant surface temperature of 340 °C in ambient air at 26 °C. This calculation resulted in a maximum vertical flow velocity of approximately 0.3 $m \cdot s^{-1}$, which, although small, may still affect received signal amplitudes, since the ultrasonic wave will be diverted away from the axis of the receiver. The magnitude of such a diversion effect was further calculated as follows. The diameter of the convective region in Fig. 4(b) traversed by the ultrasonic wave was approximately 5 mm. This means that the ultrasonic beam spends approximately 5 mm/350 $m \cdot s^{-1} = 14.3$ μs in the region of convective flow, which at a maximum vertical flow velocity of 0.3 $m \cdot s^{-1}$ would deflect the ultrasonic beam vertically by only 4 μm; quite obviously, this is negligible compared to the 10-mm transducer aperture. As a result, the dominant effects in the attenuation image of Fig. 4(a) may therefore be attributed to a combination of impedance mismatch, ray bending, and refraction arising from temperature variations, and not convective flow. Similarly for propagation delays, the flow velocity was primarily perpendicular to the velocity of the ultrasonic waves and so such effects would only become important if there were an appreciable horizontal flow component.[30] Therefore, Eq. (7) should be a good approximation, since the changes in propagation delay used to produce the slowness image in Fig. 4(b) were predominantly due to the increased air temperature as described by Eq. (4), and not changes in flow speed.

2. Reconstructing temperature fields from ultrasonic slowness fields

The ultrasonic slowness data of Fig. 4(b) was further converted to a tomographic image of temperature within the image plane, by means of Eqs. (4) and (7). Using an ambient air temperature of 26 °C (299.16 K) and thus an ambient air sound velocity of 347 $m \cdot s^{-1}$, a temperature image in °C of the scan area was reconstructed as depicted in Fig. 4(c). Here it can be seen that the maximum reconstructed air temperature at a height of 10 mm occurred immediately over the tip center and was 126.5 °C. Once again, values less than the ambient temperature were a result of noise introduced during the reconstruction.

In order to verify the reconstructed temperatures in Fig. 4(c), the air temperature was independently measured using a 1-mm-diam miniature K-type thermocouple and a Maplin ''Precision Gold'' M-1300K thermometer. As the instantaneous air temperature was found to fluctuate wildly (often by 20 °C or more), an average of seven readings was taken at 20-s intervals, and a delay of 2 min was left between moving the thermocouple and taking the readings to allow the system to stabilize. Figure 5(a) shows the temperature profile measured in a line through the image plane at a distance of 10 mm above the soldering iron tip, with the tip center located at a distance of 5 mm. Figure 5(b) shows the temperature profile measured in a vertical line starting at the tip center, where the temperature can be seen to fall from 340 °C at the tip to a temperature of 134.5 °C at a height of 10 mm. It is apparent from these two figures that the air temperature does not vary with height to the same extent as with horizontal distance.

It can also be seen in Fig. 5(a) that the maximum temperature recorded in the image plane by the thermocouple was 165.4 °C directly over the center of the tip, a value somewhat higher than that produced by the ultrasonic data. However, the measurements by the thermocouple were effectively at a single point, whereas the ultrasonic measurements were averaged over a 10-mm area (i.e., both horizontally and vertically) due to the aperture size of the transducers. Therefore, in order to make a meaningful comparison, the temperature profiles measured by the thermocouple were averaged over 10-mm distances centered about the tip of the iron.

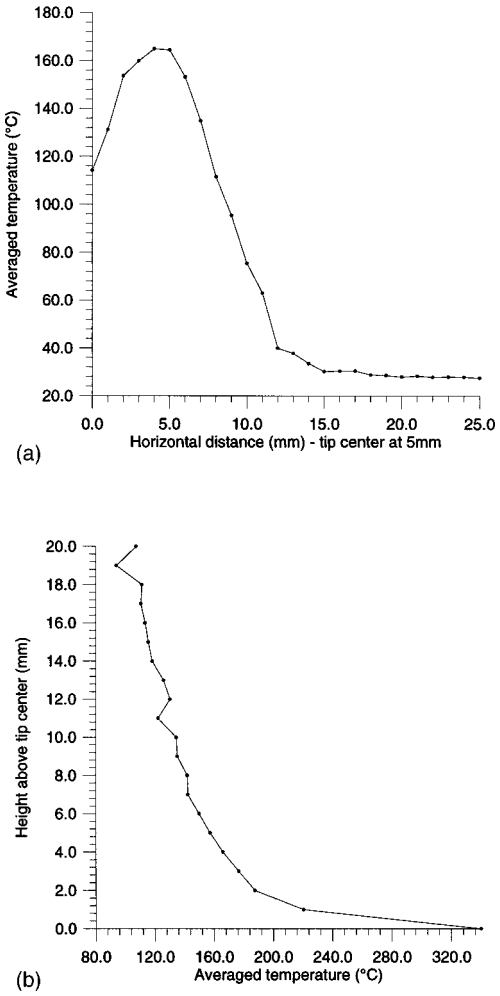

FIG. 5. (a) Horizontal and (b) vertical temperature distribution measured over the soldering iron tip with a thermocouple.

When this was done for the horizontal data of Fig. 5(a), the ''measured'' temperature by the thermocouple becomes 132.2 °C, while for the vertical data of Fig. 5(b) an average value of 133.9 °C results. As both of these average measured values are within 5% of the reconstructed temperature of 126.5 °C obtained through ultrasonic tomographic imaging, it can be concluded that the tomographic system can measure temperature profiles with reasonable accuracy. This ability of the air-coupled transducers to measure the temperature profile in air without the need to insert any object into the temperature field is an interesting application that merits further investigation.

3. Other experiments involving temperature fields

A second experiment undertaken with the single vertical soldering iron involved reconstructions at different heights above the tip. A series of five tomographic reconstructions was taken at 5-mm vertical intervals between 10 and 30 mm above the tip, and the results are shown in Fig. 6. Note that in this axial region from 10 to 30 mm, the reconstructed temperature above the iron tip varied between 131.3 °C and 87.1 °C, which is in good agreement with the thermocouple measurements, and indicates that there is very little horizontal spread in the temperature distribution with increasing

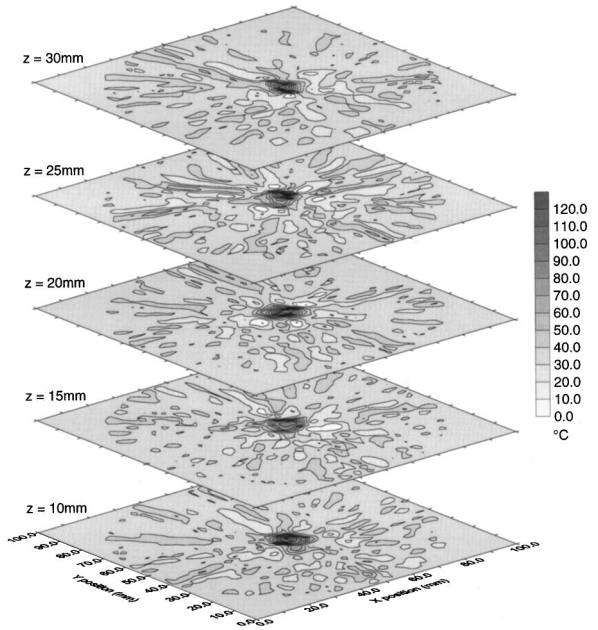

FIG. 6. Temperature images in °C at different heights z above the soldering iron.

height. This lack of horizontal temperature spread was verified by introducing a source of smoke at the tip, and observing a narrow well-defined column of heated air.

Other studies undertaken with temperature fields sought to image more complex temperature profiles. Figure 7, for example, shows the reconstructed images when two separate thermal sources were present in the scan area. A 15-W iron 3.5 mm in diameter was located in the center of the scan as before, while a 25-W iron 4.5 mm in diameter was added, offset by 20 mm in both x and y directions. The amplitude image in Fig. 7(a) in $\mathrm{dB}\cdot\mathrm{mm}^{-1}$ has clearly reconstructed the two sources, and the temperature image in Fig. 7(b) shows a larger affected area for the 4.5-mm (25-W) iron when compared to the 3.5-mm 15-W iron. There is considerable noise present in these images, however, possibly due to (a) horizontal velocity components in the air columns, (b) the use of an insufficient number of rays or projections, or (c) air turbulence caused by the close proximity of the two heat sources. Such additional sources of noise also appeared in a study that produced Fig. 8, where the 15-W iron was uninsulated and clamped horizontally to give a $3.5\times45\text{-mm}^2$ rectangular heat source. The attenuation image in $\mathrm{dB}\cdot\mathrm{mm}^{-1}$ in Fig. 8(a) does give an indication of the size and shape of the heat source, but the temperature profile in Fig. 8(b) has not been correctly reconstructed, perhaps due to the sources of noise just mentioned. Investigations are currently underway to determine the best technique required to image various types of temperature fields.

B. Imaging flow fields in air

Experiments were performed in order to verify the earlier prediction that flow fields could be imaged using ultrasonic tomography (i.e., when $|\underline{\mathbf{v}}_{\mathrm{ref}}| \gg c_{\mathrm{ref}}$ and $|\Delta\underline{\mathbf{v}}_r| \gg |\Delta c_r|$). To do so, the soldering iron was replaced by an air jet having a nozzle diameter of 1 mm and an air flow rate of 15 l/min

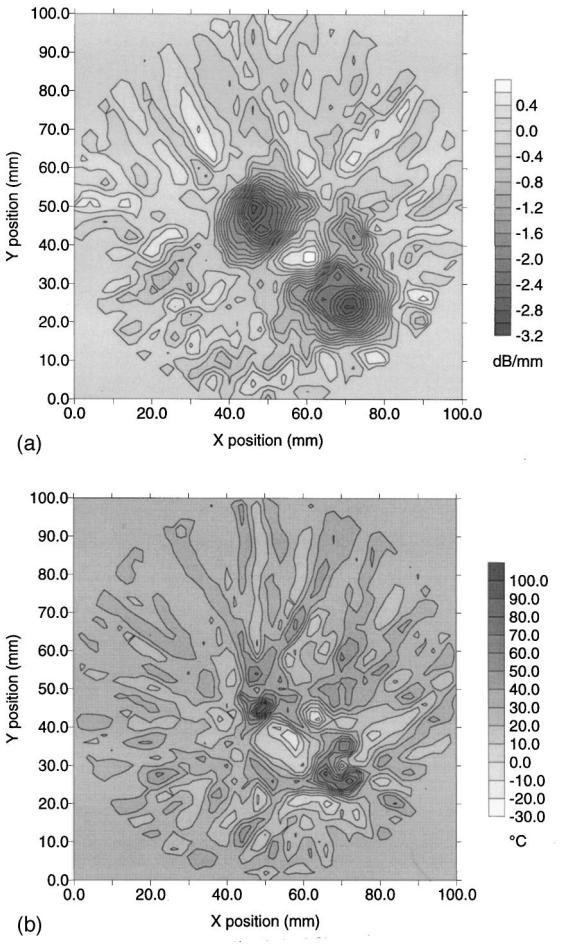

FIG. 7. (a) Attenuation image in $\mathrm{dB}\cdot\mathrm{mm}^{-1}$ and (b) temperature image in °C, taken 20 mm above two vertical soldering irons.

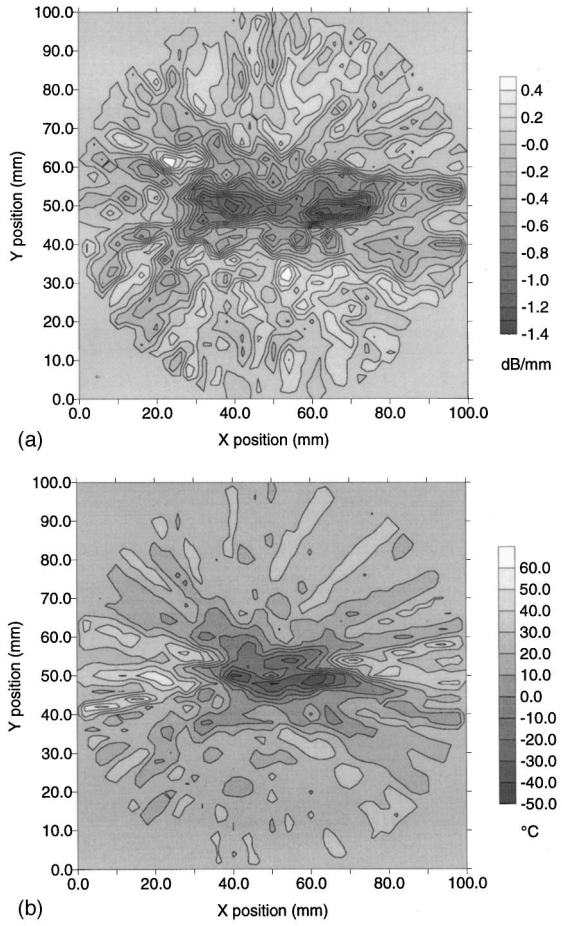

FIG. 8. (a) Attenuation image in $\mathrm{dB}\cdot\mathrm{mm}^{-1}$ and (b) temperature image in °C, taken 20 mm above a horizontal soldering iron.

(as measured using a Platon A10HS flowmeter). A tomographic scan was performed at a vertical height of 20 mm from the nozzle tip, with the scanning plane perpendicular to the direction of flow, and the results are presented in Fig. 9. Figure 9(a) shows the attenuation image in $\mathrm{dB}\cdot\mathrm{mm}^{-1}$ for the air jet, while Fig. 9(b) shows an image of the effective sound speed c_e, as reconstructed from the slowness data using a sound speed of $c_r = 347\ \mathrm{m}\cdot\mathrm{s}^{-1}$. Recall that the reconstruction of c_e in Fig. 9(b) includes only the horizontal components of the flow velocity [see Eq. (2)], which in this case will be much smaller than the vertical flow velocity of the air jet.

In order to interpret the results of Fig. 9, certain theoretical aspects of the flow-field produced by a vertical jet must be considered in some detail. For the nozzle dimension and flow rate described, the maximum vertical flow velocity at the nozzle exit (v_e) was calculated to be $319\ \mathrm{m}\cdot\mathrm{s}^{-1}$. However, the flow velocity in such a jet reduces at a rate inversely proportional to distance from the nozzle exit, and so the following semi-empirical formula[31] was used to predict the centerline flow speed v_c for a circular jet as a function of distance z from the nozzle exit:

$$\frac{v_c}{v_e} = A\frac{d}{z+a}. \tag{9}$$

In Eq. (9), d is the nozzle exit diameter, and a and A are semi-empirical constants[31] (with $A=5.9$, and a equal to either $-0.5d$ or $-3d$). For a distance $z=20$ mm above the nozzle (i.e., $20d$), Eq. (9) suggests that v_c equals either 96 or $111\ \mathrm{m}\cdot\mathrm{s}^{-1}$, depending on which value of a is used. Thus to a reasonable approximation it can be assumed that the centerline flow speed v_c will have dropped to about $100\ \mathrm{m}\cdot\mathrm{s}^{-1}$ at the scanning plane, which means that the basic assumption leading to Eq. (2) is still valid (namely $|\mathbf{v}| \leqslant 0.3c$).

It is apparent from Fig. 9(a) and (b) that the diameter of the air jet is much larger than the 1-mm diameter of the nozzle. This was not unexpected, as such an air jet is known to spread radially outwards in an approximately linear fashion with distance z from the nozzle exit, according to the following semi-empirical formula:[31]

$$\frac{d_{1/2}}{d} = \frac{z}{z_c}. \tag{10}$$

In this equation, $d_{1/2}$ is the diameter at which the flow speed has fallen to half its centerline value v_c, and z_c is the length of the so-called potential core, typically $4d$ to $5d$. As the velocity profile of the air jet is approximately Gaussian in shape, the total diameter of the jet (d_j) is actually about $2d_{1/2}$, and thus Eq. (10) gives $d_j = 0.4z$ or $0.5z$ (depending on the value of z_c). For $z=20$ mm, the beam diameter d_j is therefore expected to be approximately 8–10 mm, which is in good agreement with the reconstructed images in Fig.

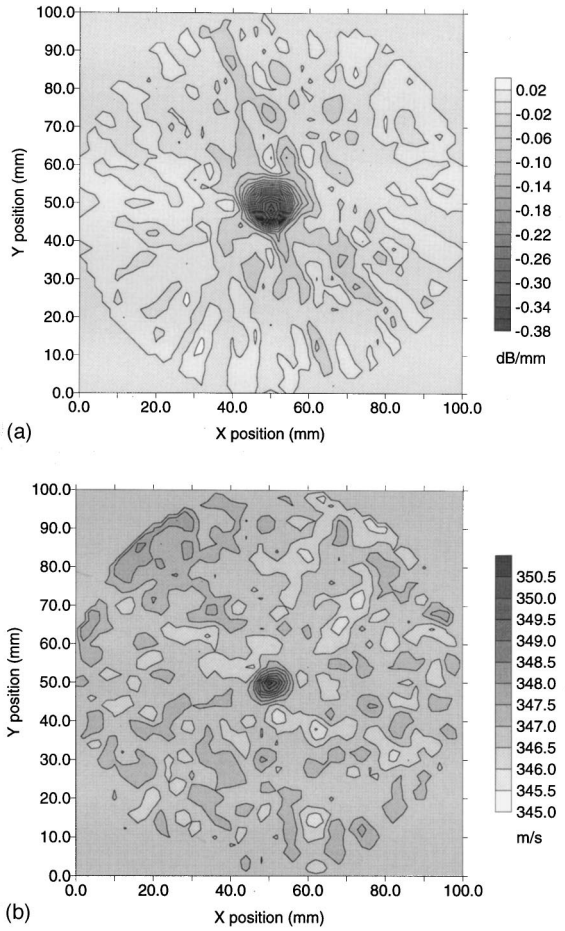

FIG. 9. (a) Attenuation image in $\mathrm{dB}\cdot\mathrm{mm}^{-1}$ and (b) velocity image in $\mathrm{m}\cdot\mathrm{s}^{-1}$ taken 20 mm above a vertical air jet.

9(a) and (b). Thus, these images clearly demonstrate that a region of high flow velocity can be successfully imaged in a gas from both ultrasonic signal amplitudes and propagation delay data.

Note that the maximum vertical flow velocity of 100 $\mathrm{m}\cdot\mathrm{s}^{-1}$ for the air jet is far higher than the convective flow velocity calculated earlier for the temperature field above the soldering iron. This means that over the 10-mm region affected by the air jet as seen in Fig. 9(a) and (b), the ultrasonic wave will have been diverted by approximately 3 mm, which is a significant offset distance when compared to the 10-mm aperture of the transducers. For this reason, the amplitude variations of Fig. 9(a) may be attributed primarily to the ultrasound being diverted away from the receiver by the flow.

It is also important to point out that the flow field will be turbulent in the case of the air jet, and so highly unsteady. Even though the flow is predominantly in the vertical direction, turbulent jets can still have instantaneous horizontal flow-velocity components that reach levels approaching $0.25v_c$.[31] The maximum horizontal component of flow velocity due to turbulence is actually expected at the jet periphery,[31] and would be of the order of 20–30 $\mathrm{m}\cdot\mathrm{s}^{-1}$ in the present case. Therefore, in principle, substantial propagation delays could be recorded by the tomographic system due to the instantaneous horizontal turbulent components. However, Fig. 9(b) was obtained from *time-averaged* propagation delay data and, accordingly, should represent the time-averaged horizontal component of the velocity field, which should be small compared with v_c. Moreover, the time-averaged horizontal flow velocity should be directed radially inward towards the vertical axis of the jet, such that for any particular ray *ab* the contributions to slowness on opposite sides of the jet would tend to cancel. A perfectly symmetric jet would not be expected to exhibit any variation in slowness. The data of Fig. 9(b) is not inconsistent with these ideas, as the measured variations in horizontal flow speeds were about 4 $\mathrm{m}\cdot\mathrm{s}^{-1}$ (i.e., only 4% of v_c), but whether Fig. 9(b) truly provides a measure of the horizontal flow components requires a more detailed future investigation. This is particularly necessary when one recalls that the flow velocity field cannot always be uniquely reconstructed from tomographic time-of-flight data for a compressible fluid (as previously discussed), and may be complicated by the existence of invisible flow.[25,26]

The need to investigate the effects of compressibility on tomographic reconstruction can further be seen in the following way. At the relatively high maximum flow speed (about 100 $\mathrm{m}\cdot\mathrm{s}^{-1}$ at the measuring plane), the variation in sound speed c_r across the jet is around 3 $\mathrm{m}\cdot\mathrm{s}^{-1}$, using estimates based on the isotropic flow relations. Accordingly, Eq. (2) is a less good approximation than at low flow speeds, such that the variation in slowness reflected in Fig. 9(b) could be explained by the variation in local sound speed owing to compressible flow effects. It is also possible that ray bending contributed to some of the measured variations in slowness. Whatever the explanation for the variations in slowness, it does appear from Fig. 9(b) that the expected dimensions of the jet (8–10 mm in diameter) are faithfully reproduced, which is a remarkable result considering the relatively large size of the transducers. Therefore, until further research is undertaken, it is safe to say that air flows can be reliably imaged tomographically by air-coupled ultrasonic transducers, but that quantitative information about the actual reconstructed parameters will not necessarily be accurate.

1. Other experiments involving flow fields

Other experiments with different flow field configurations were additionally carried out. To produce a definite measurable horizontal component of the flow velocity, the air jet was inclined at an angle of 45 degrees to the scanning plane. The flow rate was also reduced from 15 to 10 l/min, so that v_e reduced to 213 $\mathrm{m}\cdot\mathrm{s}^{-1}$. In this way elliptic, rather than circular, jet cross sections were produced. At a height of 20 mm above the nozzle exit, the jet axis cuts the scanning plane at a distance of $z=20\sqrt{2}=28.3$ mm from the nozzle. In this case Eq. (9) gives an estimated maximum flow speed v_c of approximately 45.2 to 49.7 $\mathrm{m}\cdot\mathrm{s}^{-1}$ (at 45 degrees to the scanning plane). The corresponding horizontal component should therefore be about $(47\pm2)/\sqrt{2}=33\pm1.4\,\mathrm{m}\cdot\mathrm{s}^{-1}$, and so this should be the expected range of velocity variations.

Figure 10(a) shows the reconstructed amplitude image in $\mathrm{dB}\cdot\mathrm{mm}^{-1}$ for the tilted air jet. As expected, the jet cross section is elliptical. The corresponding velocity contours, based on Eq. (8), are further plotted in Fig. 10(b). Note that the range of flow velocities obtained (about 34 $\mathrm{m}\cdot\mathrm{s}^{-1}$) is

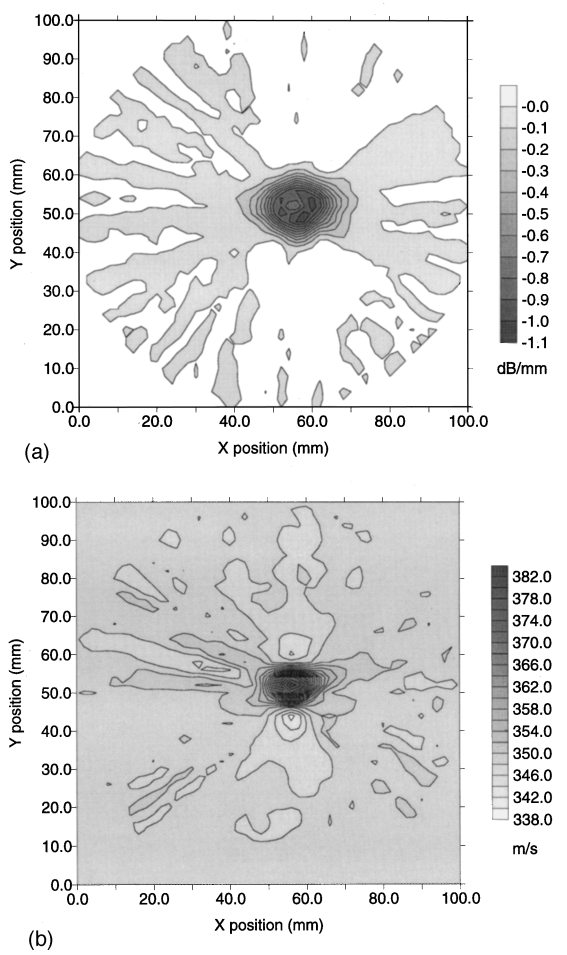

FIG. 10. (a) Attenuation image in $dB \cdot mm^{-1}$ and (b) velocity image in $m \cdot s^{-1}$ taken 20 mm above an angled air jet.

similar to the estimate given above (although compressible flow effects and ray bending may again be significant). A further selection of velocity profiles through the jet, taken at 5 mm vertical intervals between 20 and 40 mm above the nozzle tip, is included in Fig. 11. Here, the jet cross section is seen to increase in size and the velocity range reduce in amplitude as the height of the scanning plane above the nozzle is increased, as expected.

Note that a more accurate reconstruction of the flow profiles would have resulted in the above images if a full 360-degree angular range had been scanned, since this would have produced projections of slowness for ultrasound propagated both with and against the horizontal flow components. Such a method would have made it possible to either eliminate the effects of the flow or the effects of the variation in local sound speed, by adding and subtracting propagation times.[27] In principle, tomographic reconstruction of the vorticity field is also possible by this method.[28] Although this approach has not yet been employed, it will form part of future work. Nevertheless, this initial study still demonstrates the feasibility of using ultrasonic measurements in gas flows to obtain tomographic images of the flow field without the need to insert measuring devices into the flow.

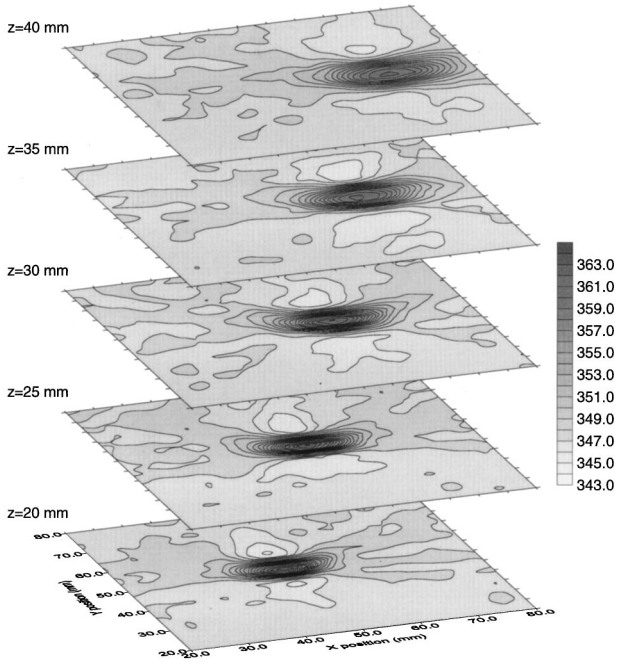

FIG. 11. Velocity images in $m \cdot s^{-1}$ at different heights z above an angled air jet.

V. CONCLUSIONS

Tomographic imaging of temperature and flow fields in air was carried out using a pair of capacitance-type ultrasonic transducers with polished metal backplates. Using a filtered back-projection algorithm and a form of difference tomography, images of both attenuation in $dB \cdot mm^{-1}$ and slowness in $ns \cdot mm^{-1}$ were obtained. The values of slowness were converted into air temperatures in °C and the temperature fields produced by commercial soldering irons were plotted at different heights above the tip. The reconstructed air temperatures were found to be in good agreement (5%) with average air temperatures measured with a miniature thermocouple. The technique was also able to resolve more than one heat source in the scan area. In terms of imaging flow fields, attenuation and velocity images were also successfully produced of cross sections through an air jet at different heights above a 1-mm-diam nozzle, and at both 90 and 45 degrees to the flow direction. In this way we have demonstrated that it is possible to use ultrasound measurements in gas flows to produce tomographic images of temperature and flow fields, without the need to insert any measuring device into the flow. Such a capability should have many interesting and useful applications.

[1] A. C. Kak and M. Slaney, *Principles of Computerized Tomographic Imaging* (IEEE, New York, 1988).
[2] H. Yamada, Y. Tomikawa, and M. Nishida, ''Application of ultrasonic computed tomography to non-destructive inspection of SiO_2 ingot material qualities,'' J. Acoust. Soc. Am. Suppl. 1 **84**, S71–S72 (1988).
[3] Y. Tomikawa, ''Non-destructive inspection of wooden poles using ultrasonic computed tomography,'' IEEE Trans. Ultrason. Ferroelectr. Freq. Control **UFFC-33**, 354–358 (1986).
[4] A. M. H. Satti and J. Szilard, ''Computerized ultrasonic tomography for testing solid propellant rocket motors,'' Ultrasonics **21**, 162–166 (1983).
[5] D. P. Jansen, D. A. Hutchins, and R. P. Young, ''Ultrasonic tomography

using scanned contact transducers,'' J. Acoust. Soc. Am. **93**, 3242–3249 (1993).
[6] T. M. Chow, D. A. Hutchins, and J. T. Mottram, ''Simultaneous acoustic emission and ultrasonic tomographic imaging in anisotropic polymer composite material,'' J. Acoust. Soc. Am. **94**, 944–953 (1993).
[7] T. Chow, D. A. Hutchins, M. D. C. Moles, and R. P. Young, ''Stress dependence of the acoustic properties of Zr-2.5 wt% Nb alloy,'' Ultrasonics **31**, 183–192 (1993).
[8] D. A. Hutchins, J. K. Hu, R. P. Young, R. Stoner, D. Jansen, and Q. L. Zhang, ''Ultrasonic tomography of metals using non-contact transduction,'' J. Acoust. Soc. Am. **85**, 747–752 (1989).
[9] D. A. Hutchins, D. P. Jansen, and C. Edwards, ''Lamb-wave tomography using non-contact transduction,'' Ultrasonics **31**, 97–103 (1993).
[10] J. K. Hu, D. A. Hutchins, J. Ungar, Q. L. Zang, and D. K. Mak, ''Non-contact ultrasonic reflection tomography,'' Mater. Eval. **47**, 736–740 (1987).
[11] D. P. Jansen, D. A. Hutchins, and J. T. Mottram, ''Lamb wave tomography of advanced composite laminates containing damage,'' Ultrasonics **32**, 83–89 (1994).
[12] H. Carr and C. Wykes, ''Diagnostic measurements in capacitive transducers,'' Ultrasonics **31**, 13–20 (1993).
[13] W. Manthey, N. Kroemer, and V. Mágori, ''Ultrasonic transducers and transducer arrays for applications in air,'' Meas. Sci. Technol. **3**, 249–261 (1992).
[14] D. W. Schindel, D. A. Hutchins, L. Zou, and M. Sayer, ''The design and characterization of micro-machined air-coupled capacitance transducers,'' IEEE Trans. Ultrason. Ferroelectr. Freq. Control **UFFC-42**, 42–50 (1995).
[15] W. M. D. Wright, D. A. Hutchins, D. P. Jansen, and D. W. Schindel, ''Air-coupled Lamb wave tomography,'' IEEE Trans. Ultrason. Ferroelectr. Freq. Control **UFFC-44**, 53–59 (1997).
[16] Y. Censor, ''Finite series expansion reconstruction techniques,'' Proc. IEEE **71**, 409–419 (1984).
[17] R. Gordon, R. Bender, and G. T. Herman, ''Algebraic reconstruction techniques for three-dimensional electron microscopy and x-ray photography,'' J. Theor. Biol. **29**, 471–481 (1970).
[18] P. Gilbert, ''Iterative methods for the three-dimensional reconstruction of an object from projections,'' J. Theor. Biol. **29**, 105–117 (1972).
[19] R. A. Kline and Y. Q. Wang, ''A technique for ultrasonic tomography in anisotropic media,'' J. Acoust. Soc. Am. **91**, 878–884 (1992).
[20] R. M. Lewitt, ''Reconstruction algorithms: transform methods,'' Proc. IEEE **71**, 390–408 (1984).
[21] H. H. Stark, J. W. Woods, I. Paul, and R. Hingorani, ''Direct Fourier reconstruction in computer tomography,'' IEEE Trans. Acoust., Speech, Signal Process. **ASSP-29**, 237–245 (1981).
[22] G. T. Herman, *Image Reconstruction from Projections: The Fundamentals of Computerized Tomography* (Academic, New York, 1980).
[23] D. P. Jansen and D. A. Hutchins, ''Immersion tomography using Rayleigh and Lamb waves,'' Ultrasonics **30**, 245–254 (1992).
[24] R. Hickling and S. P. Marin, ''The use of ultrasound for gauging and proximity sensing in air,'' J. Acoust. Soc. Am. **79**, 1151–1160 (1986).
[25] S. J. Norton, ''Tomographic reconstruction of 2-D vector fields: application to flow imaging,'' Geophys. J. **97**, 161–168 (1988).
[26] S. A. Johnson, J. F. Greenleaf, C. R. Hansen, W. F. Samayoa, M. Tanaka, A. Lent, D. A. Christensen, and R. L. Woolley, ''Reconstructing three-dimensional fluid velocity vector fields from acoustic transmission measurements,'' in *Acoustical Holography* (Plenum, New York, 1977), Vol. 7, pp. 307–326.
[27] H. Braun and A. Hauck, ''Tomographic reconstruction of vector fields,'' IEEE Trans. Signal Process. **SP-39**, 464–471 (1991).
[28] K. B. Winters and D. Rouseff, ''Tomographic reconstruction of stratified fluid flow,'' IEEE Trans. Ultrason. Ferroelectr. Freq. Control **UFFC-40**, 26–33 (1993).
[29] G. F. C. Rogers and Y. R. Mayhew, *Thermodynamic and Transport Properties of Fluids* (Blackwell, Oxford, 1995), 5th ed.
[30] J. P. Holman, *Heat Transfer* (McGraw–Hill, New York, 1986), 6th ed., pp. 323–329.
[31] J. O. Hinze, *Turbulence* (McGraw–Hill, New York, 1975), 2nd ed., pp. 535 *et seq*.